Iron stable isotopes track pelagic iron cycling during a subtropical phytoplankton bloom

Michael J. Ellwood[a,1], David A. Hutchins[b], Maeve C. Lohan[c], Angela Milne[c], Philipp Nasemann[d], Scott D. Nodder[e], Sylvia G. Sander[d], Robert Strzepek[a], Steven W. Wilhelm[f], and Philip W. Boyd[g,2]

[a]Research School of Earth Sciences, Australian National University, Canberra, ACT 2601, Australia; [b]Marine and Environmental Biology, Department of Biological Sciences, University of Southern California, Los Angeles, CA 90089; [c]School of Geography, Earth and Environmental Sciences, University of Plymouth, Plymouth PL4 8AA, United Kingdom; [d]Marine and Freshwater Chemistry, Department of Chemistry, University of Otago, Dunedin 9054, New Zealand; [e]National Institute of Water and Atmospheric Research, Wellington 6021, New Zealand; [f]Department of Microbiology, The University of Tennessee, Knoxville, TN 37996; and [g]National Institute of Water and Atmospheric Research Centre for Chemical and Physical Oceanography, Department of Chemistry, University of Otago, Dunedin 9012, New Zealand

Edited by Edward A. Boyle, Massachusetts Institute of Technology, Cambridge, MA, and approved December 1, 2014 (received for review November 11, 2014)

The supply and bioavailability of dissolved iron sets the magnitude of surface productivity for ∼40% of the global ocean. The redox state, organic complexation, and phase (dissolved versus particulate) of iron are key determinants of iron bioavailability in the marine realm, although the mechanisms facilitating exchange between iron species (inorganic and organic) and phases are poorly constrained. Here we use the isotope fingerprint of dissolved and particulate iron to reveal distinct isotopic signatures for biological uptake of iron during a GEOTRACES process study focused on a temperate spring phytoplankton bloom in subtropical waters. At the onset of the bloom, dissolved iron within the mixed layer was isotopically light relative to particulate iron. The isotopically light dissolved iron pool likely results from the reduction of particulate iron via photochemical and (to a lesser extent) biologically mediated reduction processes. As the bloom develops, dissolved iron within the surface mixed layer becomes isotopically heavy, reflecting the dominance of biological processing of iron as it is removed from solution, while scavenging appears to play a minor role. As stable isotopes have shown for major elements like nitrogen, iron isotopes offer a new window into our understanding of the biogeochemical cycling of iron, thereby allowing us to disentangle a suite of concurrent biotic and abiotic transformations of this key biolimiting element.

iron isotopes | marine biogeochemical cycles | trace metals | phytoplankton blooms | GEOTRACES

Springtime phytoplankton blooms are major contributors to the drawdown of carbon dioxide (CO_2) from the atmosphere and its sequestration into the ocean's interior (1, 2). In the context of the ocean's iron (Fe) biogeochemical cycle, spring blooms represent a transition from early season production, fueled largely by new Fe from underlying waters or lateral supply (3), to postbloom conditions where primary production is mainly (i.e., ∼90%) supported by an efficient Fe recycling loop between biogenic particulates and the dissolved Fe pool (3). Photochemical reduction and biological processing of inorganic, complexed, and particulate Fe significantly enhances Fe bioavailability (4–7); however, our understanding of the mechanisms, timing, and rates of Fe exchange between pools (dissolved, lithogenic, and biogenic) and redox species (Fe^{II} and Fe^{III}) during the onset and development of a phytoplankton bloom is limited. Indeed, the transient nature of many of these processes makes it difficult to quantify their influence on the biogeochemical cycling of Fe.

Iron isotope ratios ($^{56}Fe/^{54}Fe$) are a promising tool because isotope fractionation can occur upon transformation of Fe redox species (8), particulate dissolution (9), scavenging (10), precipitation (11), and biological uptake by phytoplankton (12). To date, a limited number of open ocean Fe isotope studies have been published (10, 12–14), with few combining both dissolved and particulate data to trace exchanges between various Fe pools. Here, we present Fe isotope data from two GEOTRACES (www.geotraces.org) process voyages (2008 and 2012) designed to study temporal changes in the biogeochemical cycling of Fe at the same locality in subtropical waters (38°S–39°S, 178°W –180°W) within the mesoscale eddy field east of New Zealand (3). We first present in situ results for dissolved and particulate Fe (DFe and PFe) cycling during the annual spring bloom, followed by the findings from a shipboard 700-L mesocosm incubation experiment, and then a conceptual model outlining the key chemical and biological processes involved in Fe isotope fractionation.

Results and Discussion

Across the two voyages, we identified three distinct stages associated with the progression of the annual spring bloom. Stage I is characterized by low Net Primary Productivity (NPP) (1.54 μmol $C{\cdot}L^{-1}{\cdot}d^{-1}$), low chlorophyll a (Chl) concentrations, low biomass (Fig. 1 and Fig. S1), and relatively homogenous nitrate and DFe profiles between 0 m and 250 m (Fig. 2*A*). This is indicative of a system that has been reset by turbulent mixing and convective overturning during winter (15) and primed, environmentally, for phytoplankton to bloom. Stage II is characterized by the initial development of a diatom-dominated bloom, increasing rates of NPP (6.15 μmol $C{\cdot}L^{-1}{\cdot}d^{-1}$) and phytoplankton and grazer biomass (Fig. 1 and Fig. S1), resulting in partial

Significance

The supply and bioavailability of dissolved iron sets the magnitude of surface productivity for approximately 40% of the global ocean; however, our knowledge of how it is transferred between chemical states and pools is poorly constrained. Here we utilize the isotopic composition of dissolved and particulate iron to fingerprint its transformation in the surface ocean by abiotic and biotic processes. Photochemical and biological reduction and dissolution of particulate iron in the surface ocean appear to be key processes in regulating its supply and bioavailability to marine biota. Iron isotopes offer a new window into our understanding of the internal cycling of Fe, thereby allowing us to follow its biogeochemical transformations in the surface ocean.

Author contributions: M.J.E., D.A.H., S.D.N., R.S., S.W.W., and P.W.B. designed research; M.J.E., M.C.L., A.M., P.N., S.D.N., S.G.S., R.S., S.W.W., and P.W.B. performed research; M.J.E. contributed new reagents/analytic tools; M.J.E., D.A.H., A.M., P.N., S.G.S., R.S., and S.W.W. analyzed data; and M.J.E., D.A.H., M.C.L., S.G.S., S.W.W., and P.W.B. wrote the paper.

The authors declare no conflict of interest.

This article is a PNAS Direct Submission.

[1]To whom correspondence should be addressed. Email: Michael.Ellwood@anu.edu.au.

[2]Present address: Institute for Marine and Antarctic Studies, University of Tasmania, Hobart, TAS 7005, Australia.

This article contains supporting information online at www.pnas.org/lookup/suppl/doi:10.1073/pnas.1421576112/-/DCSupplemental.

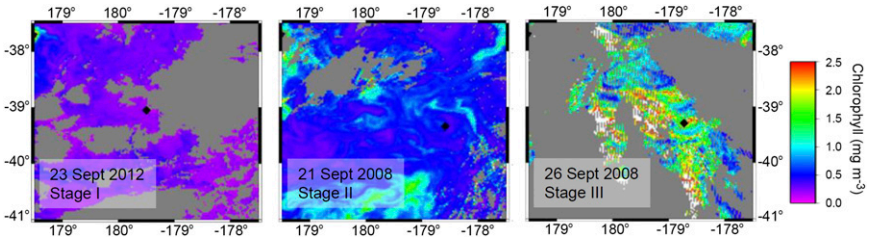

Fig. 1. Satellite-derived chlorophyll concentrations for stages I, II, and III of the subtropical spring phytoplankton bloom. Diamond represents the sampling site. Gray areas represent cloud cover during the satellite pass-over. MODIS Aqua satellite data obtained from ERDDAP and plotted using Generic Mapping Tools (46).

drawdown of nitrate and DFe within the mixed layer (Figs. 1 and 2*B*). Stage III is characterized by elevated NPP (10.7 μmol $C{\cdot}L^{-1}{\cdot}d^{-1}$), higher Chl concentrations/biomass (Fig. S1) and a corresponding biological depletion of nitrate and DFe within and immediately below the mixed layer (Figs. 1 and 2*C* and Fig. S1) (3, 16).

A time-dependent change in the δ^{56}Fe composition of DFe and PFe is observed across stages I to III (Fig. 2 and Fig. S2). During stage I, the δ^{56}Fe composition of DFe and PFe within the euphotic zone was different, with lighter δ^{56}Fe values for DFe ($\Delta^{56}Fe_{PFe\text{-}DFe} = 0.28‰$) relative to PFe (Fig. 2*D*). The dissolved δ^{56}Fe composition varied vertically whereby δ^{56}Fe values increased with depth (100–300 m), even though nitrate and the DFe profiles were homogenous (5.10 ± 0.19 μmol$\cdot L^{-1}$ and 0.38 ± 0.02 nmol$\cdot kg^{-1}$, respectively). At 300 m, the δ^{56}Fe composition of DFe and PFe was isotopically the same ($0.04 \pm 0.09‰$ and $0.08 \pm 0.01‰$, respectively) and consistent with an inferred lithogenic provenance of coastally derived particulates (Fig. 2*D* and Fig. S2) (3, 12, 16, 17).

During stage I, there are two candidate processes that could lead to an isotopically light DFe pool within the euphotic zone: photochemical and biological reduction of PFe, the latter via acidic phagocytosis upon ingestion by protozoan grazers (18–20). The key process required for δ^{56}Fe fractionation is the reduction of Fe^{III} to Fe^{II} and its subsequent release into solution; δ^{56}Fe fractionation associated with proton-promoted dissolution of lithogenic Fe (e.g., goethite and hematite), as might occur in the digestive gut of grazers, is likely to be less (9, 21) compared with δ^{56}Fe fractionation associated with photochemical reduction of lithogenic Fe. It should also be noted that acidic and enzymatic digestion of PFe by grazers may also promote Fe reduction and solubilization (20), but it is usually followed by exposure to alkaline conditions, which leads to reoxidization before egestion (20). If a portion of this reduced, isotopically light Fe is taken up by the grazer, then this would lead to an isotopically heavier Fe

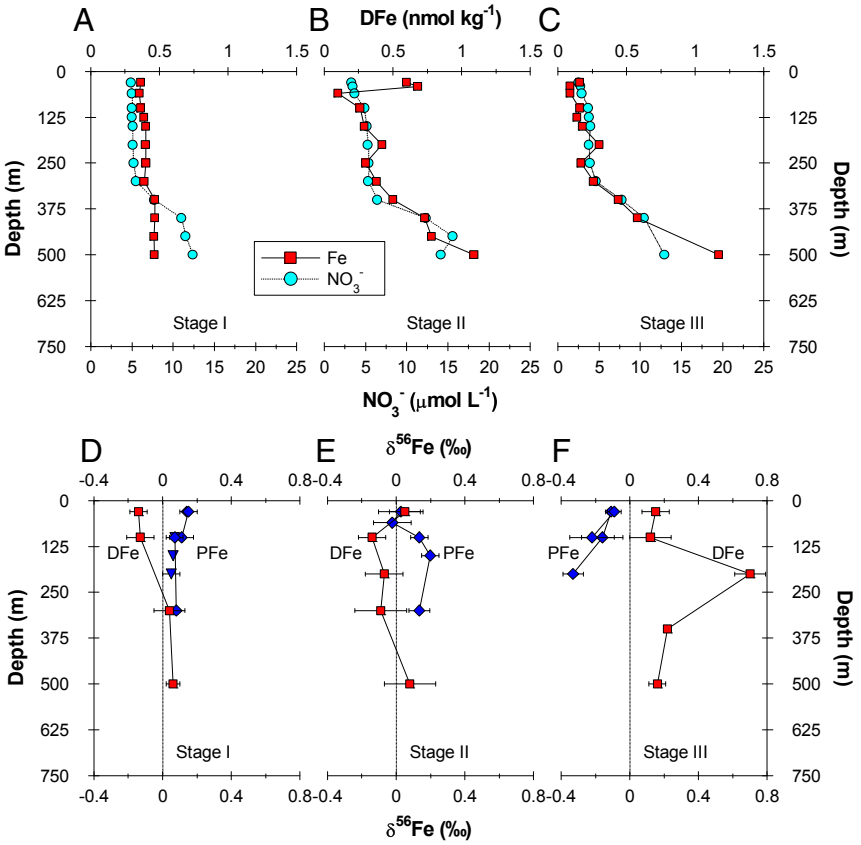

Fig. 2. DFe and δ^{56}Fe depth profiles. (*A*–*C*) Depth profiles of DFe and dissolved nitrate concentration across the three stages of the annual spring phytoplankton bloom. (*D*–*F*) The δ^{56}Fe results for dissolved, suspended (diamonds), and sinking particulates (upside-down triangles) across the three stages of the phytoplankton bloom. Error bars represent either 2 SDs for multiple sample extraction and isotope separations or 2 SEs of instrument precision for a single sample extraction and isotope separation.

composition of the remaining Fe pool upon reoxidation and loss via egestion. At this stage, we cannot fully disentangle the contributions of these two processes (photochemical versus grazer-mediated biological processing of lithogenic Fe) to the isotopically light dissolved Fe pool, but note from the information available that the photochemical reduction rate is likely to be two to three times higher than that of grazer-mediated Fe processing during stage I when grazer biomass and bacterial abundance were low (Table S1 and Fig. S1). Clearly, though, more work will be needed to distinguish between photochemical and biological effects on particulate iron dissolution and isotopic fractionation. These multiple lines of evidence (relationship between DFe and PFe, and isotopic signatures with depth) and, in particular, the low dissolved δ^{56}Fe values within the euphotic zone are consistent with the release of isotopically light Fe from lithogenic particulate material (22–25).

During the bloom onset (stage II), the δ^{56}Fe compositions of DFe and PFe within the mixed layer are the same within error ($\Delta\delta^{56}Fe_{PFe\text{-}DFe}$ = 0.05‰), indicating a biological influence on δ^{56}Fe fractionation (Fig. 2*E*). This is evident in size-fractionated plankton samples (0.2–20 μm and >20 μm) within the mixed layer, with the 0.2- to 20-μm size fraction being 0.15‰ lighter than the >20-μm size fraction (Fig. 3*A*). Pools of Fe associated with small phytoplankton are known to turn over on a timescale of hours (26); thus δ^{56}Fe fractionation in the 0.2- to 20-μm size fraction likely reflects fractionation associated with the rapid recycling of Fe between the DFe pool and biogenic components within the PFe pool. In addition, small (e.g., *Synechococcus*) and large phytoplankton (e.g., the diatom *Asterionellopsis glacialis*) may also fractionate δ^{56}Fe to differing degrees, although we did not see δ^{56}Fe fractionation between differing size classes in our mesocosm experiment (see below). Below the mixed layer, the δ^{56}Fe composition of DFe is lighter than PFe ($\Delta^{56}Fe_{PFe\text{-}DFe}$ = ~0.2‰ at 100 m) (Fig. 2*E*), which is still characteristic of a system reset by winter mixing (15), even though DFe levels are ~0.1 nmol·kg^{-1} lower than during stage I.

At the peak of the bloom (stage III), the δ^{56}Fe composition of DFe within the mixed layer is heavier than the δ^{56}Fe composition of particulate material ($\Delta^{56}Fe_{PFe\text{-}DFe}$ = −0.26‰), consistent with isotope fractionation during biological uptake (Fig. 2*F*). Below the mixed layer, the δ^{56}Fe composition of DFe is also heavier than PFe and is linked to the depletion of DFe (Fig. 2*C*); the concentration of DFe at 100 m is ~0.22 nmol·kg^{-1} lower than during bloom stage I.

The overall change in $\Delta^{56}Fe_{PFe\text{-}DFe}$ across bloom stages I to III is −0.54‰ and is indicative of δ^{56}Fe fractionation mainly associated with DFe uptake by small phytoplankton (12). The changes observed in the δ^{56}Fe composition of DFe and PFe during the evolution of the bloom are supported by changes in the particulate Fe to aluminum (Fe:Al) ratio of particulate matter and the percentage of biogenic Fe to the total PFe pool; both parameters increase across stages I to III (Fig. 3*B*).

To further interpret our field results, we conducted a 700-L phytoplankton mesocosm experiment, using water collected during bloom stage I (Fig. 4). During this time-course incubation study, fluorescence (F_0), as an indicator of Chl biomass, increased while nutrients (NO_3 and Si) and DFe were drawn down as a phytoplankton bloom developed over an 8-d period (Fig. 4). The bloom-forming diatom *Asterionellopsis glacialis* dominated biomass after day 3, which is consistent with our field results where this diatom species was also dominant (3, 16). In contrast to our field results, in the mesocosm experiment, no significant variations in the δ^{56}Fe composition of DFe or size-fractionated (0.2 μm to 2 μm, 2 μm to 20 μm, and >20 μm) PFe were observed (Fig. 4*F*). The differences between our field and mesocosm δ^{56}Fe results can be reconciled in the following ways: First, during the in situ field experiment, the Fe uptake was dominated by the 0.2- to 2-μm and 2- to 20-μm size classes (3), whereas DFe uptake in the mesocosm experiment was dominated by the >20-μm size class (Fig. 4*D*); Second, we note that the *fe* ratio (the ratio of new Fe uptake versus total uptake of new and recycled iron) declined from ~0.6 during stage II to ~0.1 during stage III of the in situ phytoplankton bloom. Because small phytoplankton dominate DFe drawdown and recycling in the in situ bloom (3) and large diatoms dominate DFe and nutrient drawdown in the mesocosm experiment (Fig. 4), the likely driver of the observed changes in δ^{56}Fe composition of DFe and PFe for the in situ phytoplankton is the uptake and regeneration of Fe by small phytoplankton (e.g., cyanobacteria) along with the export of biogenic iron to depth (16). Of course, export does not occur in the mesocosm experiment as it is a closed system. In other words, biological δ^{56}Fe fractionation associated with the in situ field experiment is likely to be coupled to the frequency with which Fe has cycled through the "ferrous wheel" by the microbial community and the amount of biogenic iron that is exported from the mixed layer (27, 28).

Scavenging and the precipitation of DFe also result in δ^{56}Fe fractionation (9, 11, 29). The contribution of this particle-mediated δ^{56}Fe fractionation was explored on a third voyage in 2011 by following changes in δ^{56}Fe for DFe as it is lost from solution from a constant hydrothermal supply source of DFe and PFe into subtropical waters (Fig. 5*A*). We note that there are caveats associated with this approach, such as the potential for the formation of multiple particulate Fe phases with differing isotope fractionation factors (11); in particular, phases formed under kinetic control have a different δ^{56}Fe composition compared with phases formed under equilibrium control (30). However,

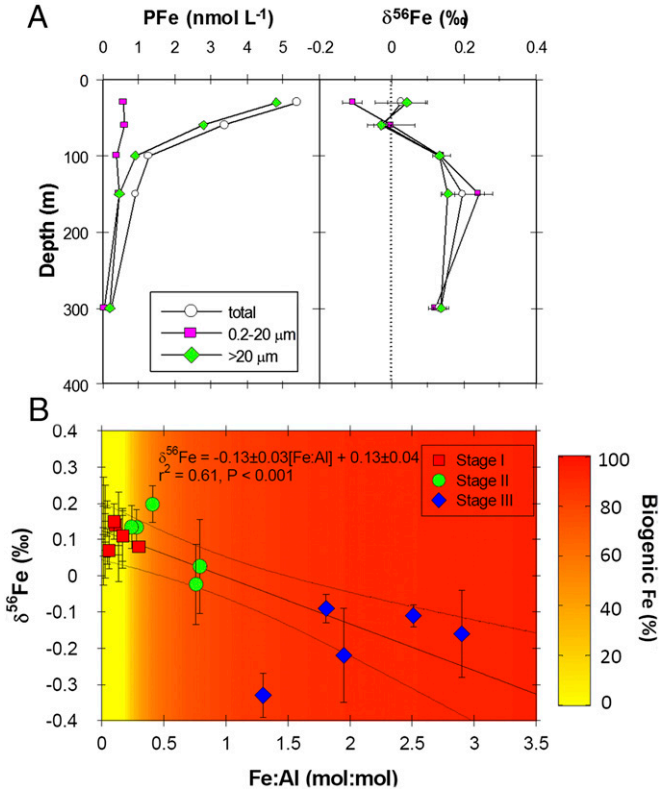

Fig. 3. Size-fractionated PFe and δ^{56}Fe depth profiles. (*A*) Depth profiles of size-fractionated (0.2–20 μm and >20 μm) PFe concentration and δ^{56}Fe. (*B*) PFe isotope versus Fe:Al ratio for suspended particulate matter across stages I to III along with the percentage of biogenic Fe for PFe. The percentage of biogenic Fe is iron is based on excess PFe relative to the lithogenic Fe:Al ratio of 0.18 (16). Error bars are the same as in Fig. 2.

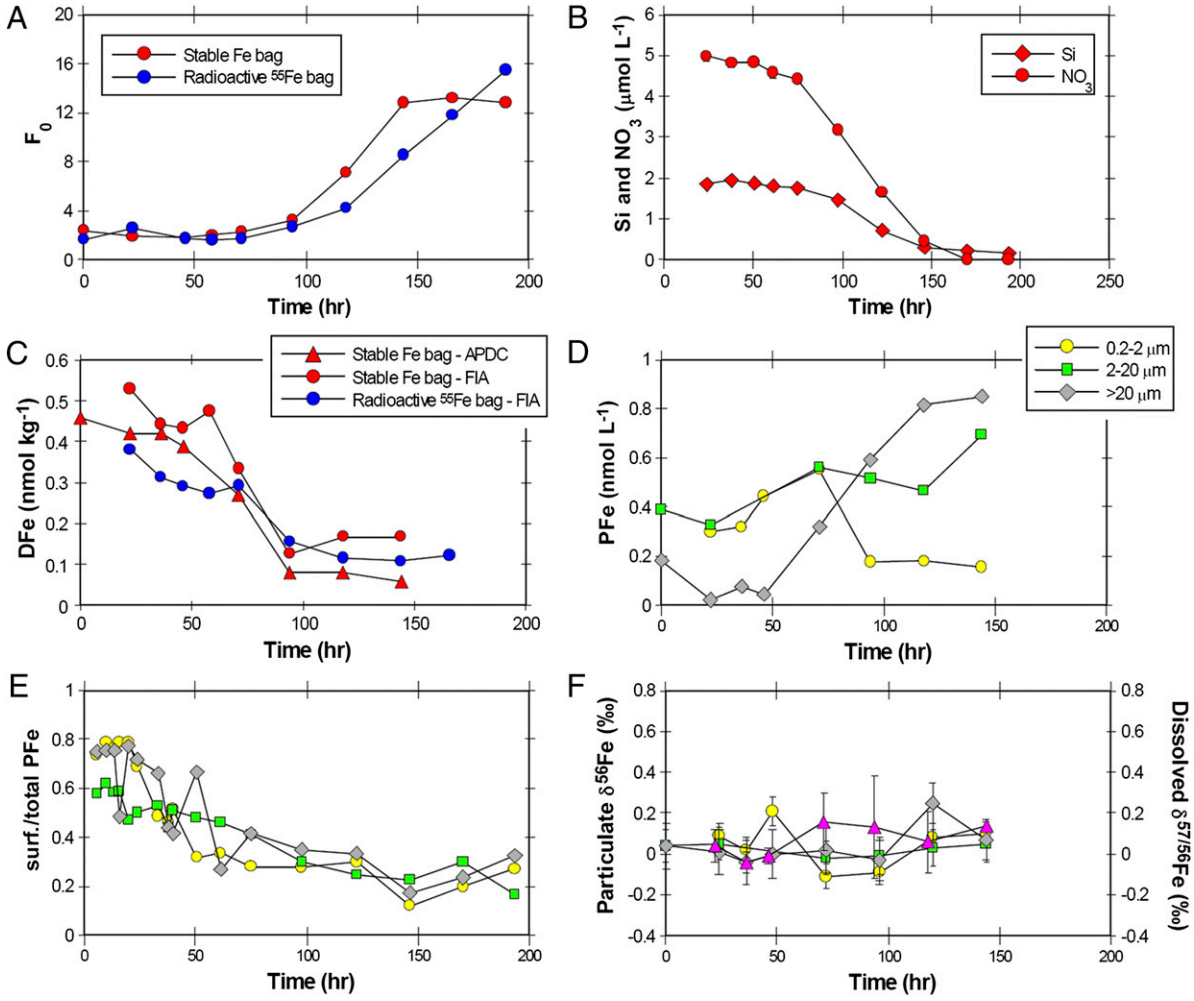

Fig. 4. DFe and PFe results for the large incubation bag mesocosm experiment. (*A*) Fluorescence (F_0) versus time for the stable and radioactive Fe bags. The increase in F_0 is consistent with an increase in plankton biomass as time progresses. (*B*) Drawdown of silicate and nitrate versus time for the stable Fe bag. (*C*) Drawdown of DFe concentration versus time for the stable and radioactive Fe bags determined by flow injection analysis and solvent extraction (see *SI Methods*). (*D*) Size-fractionated PFe concentrations for the stable bag. (*E*) Ratio of surface-absorbed Fe versus total PFe for size-fractionated particulate samples labeled with radioactive ^{55}Fe. The symbols are the same as in *D*. (*F*) Size-fractionated δ^{56}Fe data for PFe and $\delta^{57/56}$Fe for DFe (purple triangles) for the stable Fe bag. The symbols are the same as in *D*. Error bars are the same as in Fig. 2.

our approach is justified as it represents Fe isotopic fractionation under the relevant marine conditions (i.e., well-oxygenated waters at seawater pH) for DFe loss from solution by scavenging and/or mineral precipitation under abiotic conditions within the deeper water column (9). As DFe was lost from solution, its δ^{56}Fe composition increased from ∼0.07‰ to 1.73‰. Using these data we obtained a fractionation factor of −0.67‰ (Fig. 5*B*), which is similar to the change in $\Delta^{56}Fe_{PFe\text{-}DFe}$ (−0.54‰) across bloom stages I to III for our field study and within the range for Fe^{III} loss from solution (Table S1). However, in our mesocosm experiment, the percentage of Fe bound to the surface of the particulate material decreased from 60–80% at the start of the experiment to 20–40% as the mesocosm phytoplankton bloom peaked (Fig. 4). Thus, phytoplankton were actively taking up and retaining Fe. Likewise, the biological uptake of DFe during stages II and III matches that of the observed water column decrease in the mixed layer DFe inventory (3); thus the overall change in $\Delta\delta^{56}Fe_{PFe\text{-}DFe}$ across stages I to III appears to be associated with biological-induced isotope fractionation and not DFe scavenging. Below the euphotic zone, Fe release and scavenging associated with the remineralization of sinking organic matter (31) will influence the δ^{56}Fe composition of DFe and PFe.

The candidate process(s) put forward to explain the spatial and temporal trends in our δ^{56}Fe results are highlighted in a conceptual diagram (Fig. 6). At a depth of 300 m, during stage I, the two processes leading to δ^{56}Fe fractionation are desorption/dissolution and sorption/scavenging of PFe and DFe, respectively (Fig. 6*B* and Table S2). In the euphotic zone, the dominant processes leading to δ^{56}Fe fractionation are likely to be reductive dissolution of detrital/lithogenic Fe (photochemically or biologically induced) along with desorption/dissolution and sorption/scavenging processes for PFe and DFe, respectively. During stages II and III, biological uptake of DFe is likely to dominate δ^{56}Fe fractionation within the euphotic zone as DFe is taken up by phytoplankton.

Our results show that Fe cycling during the annual spring phytoplankton bloom in subtropical waters, east of New Zealand, is dynamic with photochemical reduction and biological processing of PFe appearing to play important roles in cycling Fe between the particulate and dissolved pools before bloom onset, after which the biological processing of DFe dominates (32–34). In low-Fe environments (e.g., the Southern Ocean, the southwest Pacific, and Equatorial Pacific), diel variations in the δ^{56}Fe composition of the DFe pool might be expected as a result of

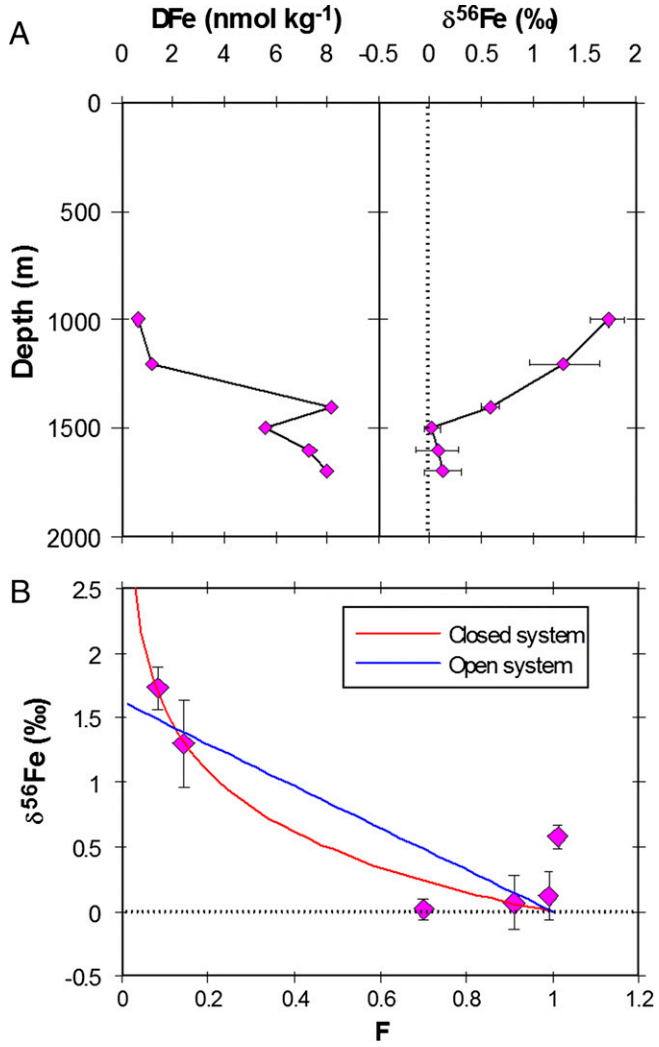

Fig. 5. Influence of particulate scavenging and mineral precipitation on DFe and δ^{56}Fe fractionation. (*A*) Depth profiles of DFe concentration and δ^{56}Fe for samples collected adjacent to the Brothers underwater volcano. Error bars are the same as in Fig. 2. (*B*) Open and closed system Rayleigh fractionation modeling (47) of δ^{56}Fe values using *A* for samples collected adjacent to the Brothers underwater volcano, where F is the fraction of DFe remaining relative to a DFe concentration of 8.31 nmol·kg^{-1}. The closed system model produces an α_{scav} = –0.67‰ while the open system model produces an α_{scav} = –1.62.

both photochemical interactions with particulate material and during biological processing (i.e., Fe recycling by grazers, viruses, and heterotrophic bacteria); however, the challenge is to extract this information, because determining the δ^{56}Fe composition DFe species at low concentrations (<0.1 nmol·L^{-1}) is nontrivial. The present study shows that iron isotopes are a valuable diagnostic tool to trace the photochemical, abiotic, and biological transformation of DFe and PFe and will form an important new component of future studies of the biogeochemical cycling of this key limiting nutrient in the ocean.

Methods

Sample Collection. Surface seawater was either collected from a depth of ~5 m using a trace-metal-free pump system (Almatec SL20) (35) or using acid-cleaned, 5-L Teflon-coated externally sprung Niskin bottles, attached to an autonomous rosette (Model 1018; General Oceanics). Seawater samples for DFe concentration and isotope measurements were filtered through acid-cleaned 0.2-μm capsule filters (Supor AcroPak 200; Pall) and acidified to pH 1.8 with Teflon-distilled nitric acid.

Particulate trace metal samples were collected in situ onto acid-leached 0.2-μm polycarbonate (142-mm diameter) filters (Nucleopore Whatman) using two large volume pumps (McLane Research Laboratories), deployed at various water depths. At a few stations, acid-leached 20-μm polycarbonate filters (Sterlitech) were also fitted to the filter stack so that two size classes were obtained: 0.2–20 μm and >20 μm. Sinking cells and particles were intercepted using surface-tethered, free-drifting MULTI-trap sediment traps deployed at 100-, 150-, and 200-m depths, which were trace metal-cleaned and preserved using a chloroform salt brine (35–38).

Hydrothermally influenced seawater samples were collected in 2011 adjacent to the Brothers underwater volcano (34°52′18.6 S, 179°03′19.8 E; northwest vent depth ~1,455 m) located along the Tonga–Kermadec arc system (39, 40) (*SI Text* and Fig. S3).

The large mesocosm experiment involved filling two acid-cleaned, 1,000-L nylon reinforced polyethylene bags (Scholle) with filtered and unfiltered surface seawater. Initially, the bags were filled with ~350 L of 0.2-μm (Acropak; Pall) filtered seawater. The bags were then spiked with either radioactive ^{55}Fe or stable Fe such that the final dissolved Fe concentration was raised by 0.2 nmol·L^{-1} to 0.45–0.5 nmol·L^{-1}. The added Fe was then allowed to equilibrate with the natural organic ligands for an 8-h period. Before dawn, each bag was then filled with unfiltered seawater containing the natural phytoplankton community to a volume of ~700 L. Bag temperatures were maintained at in situ temperature by flowing surface seawater around each incubation bag. Each bag was shaded to 50% of incident radiation. Time-course samples for each bag were collected periodically (6- to 24-h periods) for DFe, size-fractionated (0.2–2 μm, 2–20 μm, and >20 μm) particulate trace metals, DFe and PFe isotopes, and nutrients. Dissolved Fe for the radioactive ^{55}Fe or stable Fe bags were determined by flow injection analysis with chemiluminescence detection of Fe using luminol following trace element preconcentration on to the Toyopearl AF-Chelate-650 M resin (Tosoh Bioscience) (41, 42).

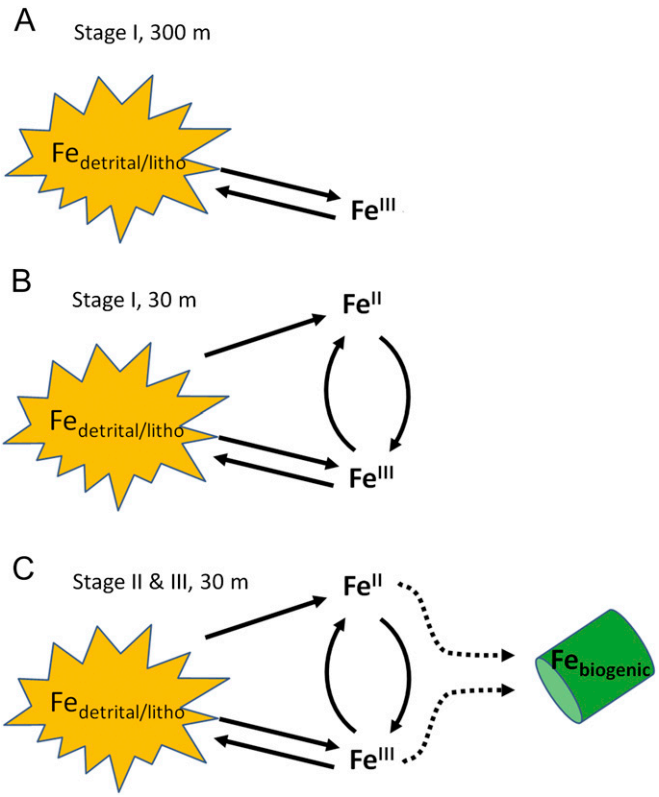

Fig. 6. Cartoon highlighting the various pathways that can lead to δ^{56}Fe fractionation. (*A*) Stage I, depth of 300 m. (*B*) Stage I, euphotic zone. (*C*) Stages II and III, euphotic zone. For simplicity, no differentiation between inorganic Fe and Fe complexation to natural organic ligands was made; rather, we treated inorganic Fe and organically complexed Fe as one group. Water column measurements from both the 2008 and the 2012 voyages indicate that the majority (>90%) of DFe was complexed to high-affinity Fe-binding ligands (FeL) (3).

The background PFe concentration at the start of the mesocosm experiment was estimated to be between 0.6 nmol·L^{-1} and 0.8 nmol·L^{-1}, which is consistent with the measured concentration range PFe within the mixed layer (0.77 nmol·L^{-1} to 1.87 nmol·L^{-1}).

Sample Analysis. Sediment trap and particulate samples for trace element and δ^{56}Fe determination were thawed and processed using the acid digestion protocol of Eggimann and Betzer (43) as described by Ellwood et al. (16).

The δ^{56}Fe composition of Fe was made on samples purified using the anion exchange procedure described by Poitrasson and Freydier (44). Before purification, DFe samples were preconcentrated by dithocarbamate extraction (16). Iron isotopes were determined using a Neptune Plus multicollector Inductively Coupled Plasma Mass Spectrometer (ICPMS) (Thermo Scientific) with an APEX-IR introduction system (Elemental Scientific) and with X-type skimmer cones. Samples were measured in high-resolution mode with ^{54}Cr interference correction on ^{54}Fe and with instrumental mass bias correction using nickel (44). Sample ^{56}Fe/^{54}Fe ratios are reported in delta notation (‰) relative to the IRMM-014 Fe isotope reference material [Institute for Reference Materials and Measurements (IRMM)] using the standard-sample-standard bracketing technique where $\delta^{56}\text{Fe} = [(^{56}\text{Fe}/^{54}\text{Fe})_{\text{sample}}/(^{56}\text{Fe}/^{54}\text{Fe})_{\text{IRMM-014}} - 1]\cdot 1{,}000$.

The overall sample processing and instrumental error for dissolved and particulate Fe samples ranged between ±0.05‰ and ±0.22‰ (2σ). The δ^{56}Fe values obtained for the GEOTRACES standards GSI and GDI and standard reference materials, BCR-2 and NOD-A-1, were within the range of published values (Table S3) for the GEOTRACES intercalibration study (45). Our particulate and dissolved δ^{56}Fe measurements were correlated to δ^{57}Fe with a δ^{57}Fe/δ^{56}Fe slope of 1.50 ± 0.03 (± std. error, $n = 147$, $P < 0.001$), which is within error of the theoretical mass-dependent fractionation slope of 1.47, except for the DFe samples for the large mesocosm experiment; hence we express these values as $\delta^{56/57}$Fe because of an interference on mass ^{54}Fe. Unfortunately, the remaining sample volume was not enough to repeat the extraction process.

ACKNOWLEDGMENTS. We thank the Captain and crew of the RV *Tangaroa* for assistance at sea, and Sarah Searson and Lisa Northcote [both from National Institute of Water and Atmospheric Research (NIWA)] for sediment trap and McLane pump deployments and sample processing. We are grateful to Ed Boyle for sharing GEOTRACES standards GSI and GDI with us. We thank two reviewers and the editor for their constructive reviews. This research was supported by the New Zealand Foundation for Research, Science and Technology Coasts and Oceans Outcome-Based Investment (CO1X0501, now NIWA Core funding), the Australian Research Council (DP110100108, DP0770820, and DP130100679), US National Science Foundation (OCE 0825405/0825319, awarded to D.A.H. and S.W.W.), Royal Society of New Zealand Marsden Fund (U001117, awarded to S.G.S.), and the National Environmental Research Council (NERC NE/H004475/1, awarded to M.C.L.).

1. Falkowski PG, Raven JA (2007) *Aquatic Photosynthesis* (Princeton Univ Press, Princeton, NJ), 2nd Ed.
2. Mahadevan A, D'Asaro E, Lee C, Perry MJ (2012) Eddy-driven stratification initiates North Atlantic spring phytoplankton blooms. *Science* 337(6090):54–58.
3. Boyd PW, et al. (2012) Microbial control of diatom bloom dynamics in the open ocean. *Geophys Res Lett* 39(18):L18601.
4. Barbeau K, Rue EL, Bruland KW, Butler A (2001) Photochemical cycling of iron in the surface ocean mediated by microbial iron(III)-binding ligands. *Nature* 413(6854): 409–413.
5. Finden DAS, Tipping E, Jaworski GHM, Reynolds CS (1984) Light-induced reduction of natural iron(III) oxide and its relevance to phytoplankton. *Nature* 309(5971):783–784.
6. Sunda WG, Huntsman SA (1997) Interrelated influence of iron, light and cell size on marine phytoplankton growth. *Nature* 390(6658):389–392.
7. Barbeau K, Moffett JW, Caron DA, Croot PL, Erdner DL (1996) Role of protozoan grazing in relieving iron limitation of phytoplankton. *Nature* 380(6569):61–64.
8. Welch SA, Beard BL, Johnson CM, Braterman PS (2003) Kinetic and equilibrium Fe isotope fractionation between aqueous Fe(II) and Fe(III). *Geochim Cosmochim Acta* 67(22):4231–4250.
9. Skulan JL, Beard BL, Johnson CM (2002) Kinetic and equilibrium Fe isotope fractionation between aqueous Fe(III) and hematite. *Geochim Cosmochim Acta* 66(17): 2995–3015.
10. John SG, Adkins J (2012) The vertical distribution of iron stable isotopes in the North Atlantic near Bermuda. *Global Biogeochem Cycles* 26(2):GB2034.
11. Beard BL, Johnson CM (2004) Fe isotope variations in the modern and ancient Earth and other planetary bodies. *Rev Mineral Geochem* 55(1):319–357.
12. Radic A, Lacan F, Murray JW (2011) Iron isotopes in the seawater of the equatorial Pacific Ocean: New constraints for the oceanic iron cycle. *Earth Planet Sci Lett* 306(1-2):1–10.
13. Lacan F, et al. (2008) Measurement of the isotopic composition of dissolved iron in the open ocean. *Geophys Res Lett* 35(L2):L24610.
14. Conway TM, John SG (2014) Quantification of dissolved iron sources to the North Atlantic Ocean. *Nature* 511(7508):212–215.
15. Tagliabue A, et al. (2014) Surface-water iron supplies in the Southern Ocean sustained by deep winter mixing. *Nat Geosci* 7(4):314–320.
16. Ellwood MJ, et al. (2014) Pelagic iron cycling during the subtropical spring bloom, east of New Zealand. *Mar Chem* 160:18–33.
17. Beard BL, Johnson CM, Von Damm KL, Poulson RL (2003) Iron isotope constraints on Fe cycling and mass balance in oxygenated Earth oceans. *Geology* 31(7):629–632.
18. Wells ML, Mayer LM (1991) The photoconversion of colloidal iron oxyhydroxides in seawater. *Deep Sea Res Part A* 38(11):1379–1395.
19. Barbeau KA, Moffett JW (1998) Dissolution of iron oxides by phagotrophic protists: Using a novel method to quantify reaction rates. *Environ Sci Technol* 32(19): 2969–2975.
20. Hutchins DA, Bruland KW (1994) Grazer-mediated regeneration and assimilation of Fe, Zn and Mn from planktonic prey. *Mar Ecol Prog Ser* 110(2-3):259–269.
21. Wiederhold JG, et al. (2006) Iron isotope fractionation during proton-promoted, ligand-controlled, and reductive dissolution of Goethite. *Environ Sci Technol* 40(12): 3787–3793.
22. Sulzberger B, Laubscher H (1995) Reactivity of various types of iron(III) (hydr)oxides towards light-induced dissolution. *Mar Chem* 50(1-4):103–115.
23. Borer P, Sulzberger B, Hug SJ, Kraemer SM, Kretzschmar R (2009) Photoreductive dissolution of iron(III) (hydr)oxides in the absence and presence of organic ligands: Experimental studies and kinetic modeling. *Environ Sci Technol* 43(6):1864–1870.
24. Waite TD, Morel FMM (1984) Photoreductive dissolution of colloidal iron oxide: Effect of citrate. *J Colloid Interface Sci* 102(1):121–137.
25. Wells ML, Mayer LM, Donard OFX, de Souza Sierra MM, Ackelson SG (1991) The photolysis of colloidal iron in the oceans. *Nature* 353(6341):248–250.
26. Poorvin L, Rinta-Kanto JM, Hutchins DA, Wilhelm SW (2004) Viral release of iron and its bioavailability to marine plankton. *Limnol Oceanogr* 49(5):1734–1741.
27. Kirchman DL (1996) Microbial ferrous wheel. *Nature* 383(6598):303–304.
28. Strzepek RF, et al. (2005) Spinning the "Ferrous Wheel": The importance of the microbial community in an iron budget during the FeCycle experiment. *Global Biogeochem Cycles* 19(4):GB4S26.
29. Anbar AD (2004) Iron stable isotopes: Beyond biosignatures. *Earth Planet Sci Lett* 217(3-4):223–236.
30. Johnson CM, Beard BL (2006) Fe isotopes: An emerging technique for understanding modern and ancient biogeochemical cycles. *GSA Today* 16(11):4–10.
31. Twining BS, et al. (2014) Differential remineralization of major and trace elements in sinking diatoms. *Limnol Oceanogr* 59(3):689–704.
32. Weber L, Völker C, Schartau M, Wolf-Gladrow DA (2005) Modeling the speciation and biogeochemistry of iron at the Bermuda Atlantic Time-series Study site. *Global Biogeochem. Cycles* 19(1):GB1019.
33. Shaked Y, Kustka AB, Morel FMM, Erel Y (2004) Simultaneous determination of iron reduction and uptake by phytoplankton. *Limnol Oceanogr Methods* 2:137–145.
34. Barbeau K (2006) Photochemistry of organic iron(III) complexing ligands in oceanic systems. *Photochem Photobiol* 82(6):1505–1516.
35. Frew RD, et al. (2006) Particulate iron dynamics during FeCycle in subantarctic waters southeast of New Zealand. *Global Biogeochem Cycles* 20(1):GB1S93.
36. Karl DM, et al. (1996) Seasonal and interannual variability in primary production and particle flux at Station ALOHA. *Deep Sea Res Part II* 43(2-3):539–568.
37. Knauer GA, Martin JH, Bruland KW (1979) Fluxes of particulate carbon, nitrogen, and phosphorus in the upper water column of the northeast Pacific. *Deep Sea Res Part A* 26(1A):97–108.
38. Martin JH, et al. (1983) *Vertical Transport and Exchange of Materials in the Upper Waters of the Oceans (VERTEX): Introduction to the Program, Hydrographic Conditions and Major Component Fluxes During VERTEX I* (Moss Landing Marine Lab, Moss Landing, CA), Tech. Publ. 83-2.
39. de Ronde CEJB, et al. (2007) Submarine hydrothermal activity along the mid-Kermadec Arc, New Zealand: Large-scale effects on venting. *Geochem Geophys Geosyst* 8(7):Q07007.
40. Massoth GJ, et al. (2003) Chemically rich and diverse submarine hydrothermal plumes of the southern Kermadec volcanic arc (New Zealand). *Geol Soc Spec Publ* 219(1): 119–139.
41. Obata H, Karatani H, Nakayama E (1993) Automated determination of iron in seawater by chelating resin concentration and chemiluminescence detection. *Anal Chem* 65(11):1524–1528.
42. de Jong JTM, et al. (1998) Dissolved iron at subnanomolar levels in the Southern Ocean as determined by ship-board analysis. *Anal Chim Acta* 377(2-3):113–124.
43. Eggimann DW, Betzer PR (1976) Decomposition and analysis of refractory oceanic suspended materials. *Anal Chem* 48(6):886–890.
44. Poitrasson F, Freydier R (2005) Heavy iron isotope composition of granites determined by high resolution MC-ICP-MS. *Chem Geol* 222(1-2):132–147.
45. Boyle EA, et al. (2012) GEOTRACES IC1 (BATS) contamination-prone trace element isotopes Cd, Fe, Pb, Zn, Cu, and Mo intercalibration. *Limnol Oceanogr Methods* 10: 653–665.
46. Wessel P, Smith WHF (1998) New, improved version of generic mapping tools released. *Eos Trans AGU* 79(47):579–579.
47. Varela DE, Pride CJ, Brzezinski MA (2004) Biological fractionation of silicon isotopes in Southern Ocean surface waters. *Global Biogeochem Cycles* 18(1):GB1047.